



Intrinsic instabilities in X-point geometry: A tool to understand and predict the Scrape Off Layer transport in standard and advanced divertors

F. Militello^{*,1}, Y. Liu

CCFE, Culham Science Centre, Abingdon, Oxon OX14 3DB, UK



ARTICLE INFO

Article history:

Available online 1 November 2014

ABSTRACT

Intrinsic Scrape Off Layer (SOL) instabilities are studied using flute approximation and incorporating the appropriate sheath boundary conditions at the target. The linear growth rate and the structure of the modes are obtained. The associated diffusion is estimated using a γ/k_{\perp}^2 approach for the fastest growing modes. The model used includes curvature and sheath drives, finite Larmor radius effects and partial line tying at the target. The magnetic geometry is obtained using current carrying wires, representing the plasma current and the divertor coils, and naturally generates X-point geometry and magnetic shear effects. The calculation is performed for ITER relevant parameters and scans in SOL width and distance from the separatrix are presented. In addition to a standard Lower Single Null, Super-X and Snowflake configurations are examined in order to assess the importance of the geometry on the stability of the boundary plasma.

© 2014 EURATOM/CCFE Fusion Association. Published by Elsevier B.V. All rights reserved.

1. Introduction

Future magnetic fusion experiments will operate under the stringent constraint posed by the interaction between plasma and solid surfaces [1,2]. Current experimental extrapolations for the heat flux Scrape Off Layer (SOL) width in ITER predict a 0.1 cm thickness at the outer midplane in the inter-ELM phase at low and medium collisionality [3]. Such sharp gradients might induce or strengthen SOL instabilities, which could enhance perpendicular turbulent transport and consequently flatten the SOL profiles. However, the mechanisms governing the perpendicular particle and energy transport in the SOL are not yet completely clarified. For example, there might be competition between local (diffusive) and nonlocal (intermittent) transport, which might contribute at different levels to the total fluxes [4,5]. The transport might also radically change in different regions of the plasma, e.g. being more intermittent upstream and more diffusive at the target. This could be due to the large variation of the equilibrium quantities in the SOL in collisional regimes [6] or to the disconnection between upstream and downstream physics due to the strong magnetic shear at the X-point [7].

While an accepted and consistent theoretical framework to describe the anomalous transport is not available, most SOL modelling codes employ a somewhat oversimplified treatment of the perpendicular dynamics of the plasma. It is common practice to assume a simple diffusive model with a diffusion coefficient independent from the magnetic geometry and spatially homogeneous, and use it as a fitting parameter to match the experimental data. These approximations leave uncertainties on the reliability of the predictions for ITER and DEMO.

In this paper, we estimate the perpendicular diffusion coefficients by identifying some of the sources of anomalous transport (the intrinsic instabilities in the SOL) and by determining their growth rate and wave number. Our work is largely based on the flute approximation as proposed in several theoretical papers [8–10] and well summarized in [10]. The stability of a single field line is considered and the structure and complex frequency of the unstable modes associated to it are obtained. The calculation is carried out for an ITER class device and repeated for field lines at different distances from the separatrix, for different SOL widths and for different divertor concepts (Lower Single Null, exact Snowflake [11], Super-X [12]) in order to assess the influence of the magnetic geometry on the stability of the SOL. While ITER baseline scenario requires partial detachment, we focus on low collisionality regimes which lead to sheath limited conditions. This is motivated by the fact that some of the results in [3] were obtained

* Corresponding author.

E-mail address: fulvio.militello@ccfe.ac.uk (F. Militello).

¹ Presenting author.

Table 1

Parameters of the current carrying wires.

	y_p	x_{d1}	y_{d1}	α_1	x_{d2}	y_{d2}	α_2
LSN	0.5	0	−0.25	0.5	/	/	/
SF	0.57	0.139	−0.114	0.25	−0.139	−0.114	0.25
SX	0.535	0.125	−0.339	0.5	−0.129	−0.154	0.15

in such a regime although the ITER divertor is expected to work in partial detachment [13].

2. Model and equations

Our calculations were carried out using an ideal drift-fluid model which includes curvature, finite Larmor radius effects, finite magnetic shear and sheath boundary conditions. The starting normalized equations are the vorticity equation, parallel Ohm's law, particle and energy conservation:

$$\frac{\partial U}{\partial t} + (\mathbf{b} \times \nabla_{\perp} \phi + \tau \mathbf{b} \times \nabla_{\perp} n) \cdot \nabla_{\perp} U = \nabla_{\parallel} J_{\parallel} + \frac{2}{\delta} \mathbf{b} \times \boldsymbol{\kappa} \cdot \nabla_{\perp} p_{tot}, \quad (1)$$

$$\frac{\partial \psi}{\partial t} + \nabla_{\parallel} \phi = \nabla_{\parallel} p + \alpha \nabla_{\parallel} T, \quad (2)$$

$$\frac{\partial n}{\partial t} + \mathbf{b} \times \nabla_{\perp} \phi \cdot \nabla_{\perp} n = 0, \quad (3)$$

$$\frac{\partial T}{\partial t} + \mathbf{b} \times \nabla_{\perp} \phi \cdot \nabla_{\perp} T = 0, \quad (4)$$

where $U \equiv \nabla_{\perp}^2 \phi$, $J_{\parallel} \equiv -\nabla_{\perp}^2 \psi$, τ is the ratio between ion and electron temperature, $p_{tot} = p_i + p_e = (\tau + 1)nT$ and $p = nT$. The normalizations are as follows: $x \equiv \hat{x} \frac{1}{R}$ for the lengths, $t \equiv \hat{t} \frac{v_A}{R}$ for the time, $\phi \equiv \hat{\phi} \frac{c}{B v_A R}$ for the electrostatic potential, $\psi \equiv \hat{\psi} \frac{1}{BR}$ for the magnetic flux, $J_{\parallel} \equiv \hat{J}_{\parallel} \frac{4\pi R}{cB}$ for the parallel current density, $p \equiv \hat{p} \frac{\delta \beta}{n_0 T_0}$ for the pressure, $n \equiv \hat{n} \frac{\delta \beta}{n_0}$ for the density, $T \equiv \hat{T} \frac{1}{T_0}$ for the electron temperature, $\boldsymbol{\kappa} \equiv \hat{\boldsymbol{\kappa}} R$ for the curvature vector, $U \equiv \hat{U} \frac{R}{v_A}$ for the vorticity.

Note that v_A is the Alfvén speed, R is the major radius, B and \mathbf{b} are the amplitude and unity vector of the confining magnetic field, $\delta = c/(R\omega_{pi})$ the normalized ion skin depth, $\alpha = 0.71\beta\delta$, $\beta = 4\pi n_0 T_0/B^2$ (note the different definition of β), n_0 and T_0 are typical values of the density and electron temperature while the ion temperature is constant. These equations contain most of the physics used in previous investigation of SOL stability (see e.g. [10] and references therein).

Using the flute approximation (i.e. $k_{\parallel} \ll k_{\perp}$) for the perturbations and assuming no parallel variations of the equilibrium we can write: $f = f_{eq}(\mathbf{x}_{\perp}) + \tilde{f}(s)e^{i(\mathbf{k}_{\perp} \cdot \mathbf{x}_{\perp} - \omega t)}$, where s is the parallel coordinate along a field line, and then linearize the system. After some algebra we obtain:

$$\frac{1}{k_{\perp}^2} \nabla_{\parallel,0} (k_{\perp}^2 \nabla_{\parallel,0} \tilde{\phi}) + [(\tilde{\omega} - \omega_{*ip})\tilde{\omega} + \gamma_{MHD}^2] \tilde{\phi} = 0, \quad (5)$$

where $\omega_E \equiv \mathbf{k}_{\perp} \cdot \mathbf{b}_0 \times \nabla_{\perp} \phi_{eq}$, $\omega_{*en} \equiv -\mathbf{k}_{\perp} \cdot \mathbf{b}_0 \times \nabla_{\perp} n_{eq}$, $\omega_{*eT} \equiv -\mathbf{k}_{\perp} \cdot \mathbf{b}_0 \times \nabla_{\perp} T_{eq}$, $\omega_{*ip} \equiv +\mathbf{k}_{\perp} \cdot \mathbf{b}_0 \times \nabla_{\perp} p_{i,eq} = -\tau \omega_{*en}$, $\tilde{\omega} \equiv \omega - \omega_E$ and $\gamma_{MHD}^2 \equiv \frac{1}{k_{\perp}^2} (\frac{2}{\delta} \mathbf{k}_{\perp} \cdot \mathbf{b}_0 \times \boldsymbol{\kappa})(\mathbf{k}_{\perp} \cdot \mathbf{b}_0 \times \nabla_{\perp} p_{tot,eq})$.

This equation needs two boundary conditions, which are given by the continuity of the plasma current at the entrance of the Debye sheath. The perturbed current from upstream is easily obtained from $\tilde{\psi} = -\frac{i}{\omega} \nabla_{\parallel,0} \tilde{\phi}$, $\tilde{n} = \frac{\omega_{*en}}{\omega} \tilde{\phi}$. The linear perturbed part of the sheath current is given by [9]: $\tilde{J}_{sh} = \sigma \frac{\sqrt{\beta}}{\rho^2} (\tilde{\phi} - \Lambda \beta \delta \tilde{T})$, where $\rho = \delta \sqrt{\beta}$ is the hybrid Larmor radius, $\Lambda \equiv -0.5 \log[2\pi(m_e/m_i)(T_i/T_e)] \approx -2.5$ is the wall floating potential and $\sigma = \pm 1$ and depends on the $\mathbf{b}_0 \cdot \mathbf{n}$ where \mathbf{n} is the unity vector perpendicular to the target surface. If the magnetic field is entering the surface $\sigma = 1$, while if it is leaving it, $\sigma = -1$. Equating these two currents gives:

$$-ik_{\perp}^2 \nabla_{\parallel,0} \tilde{\phi} = \sigma \frac{\sqrt{\beta}}{\rho^2} (\tilde{\omega} - \Lambda \beta \delta \omega_{*eT}) \tilde{\phi} \approx \sigma \frac{\sqrt{\beta}}{\rho^2} \omega \tilde{\phi} \quad (6)$$

where we used: $\omega_E \approx -\Lambda \beta \delta \omega_{*eT}$ [9].

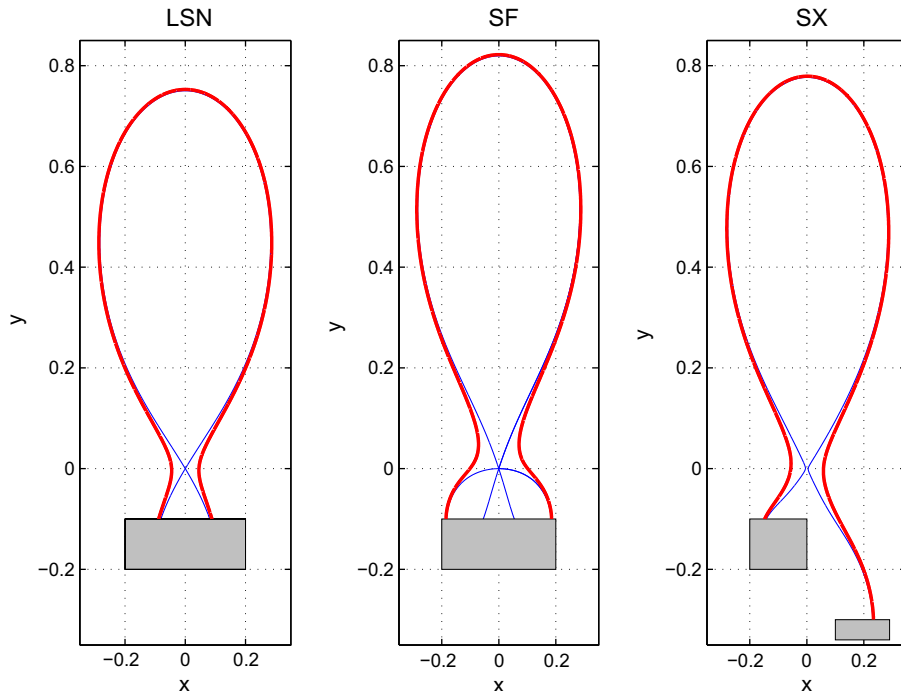


Fig. 1. Magnetic geometry of the divertor configurations studied. The thin line is the separatrix and the thick line tracks a field line 1 cm away from the separatrix at the outer midplane. Lengths are normalized with respect to R .

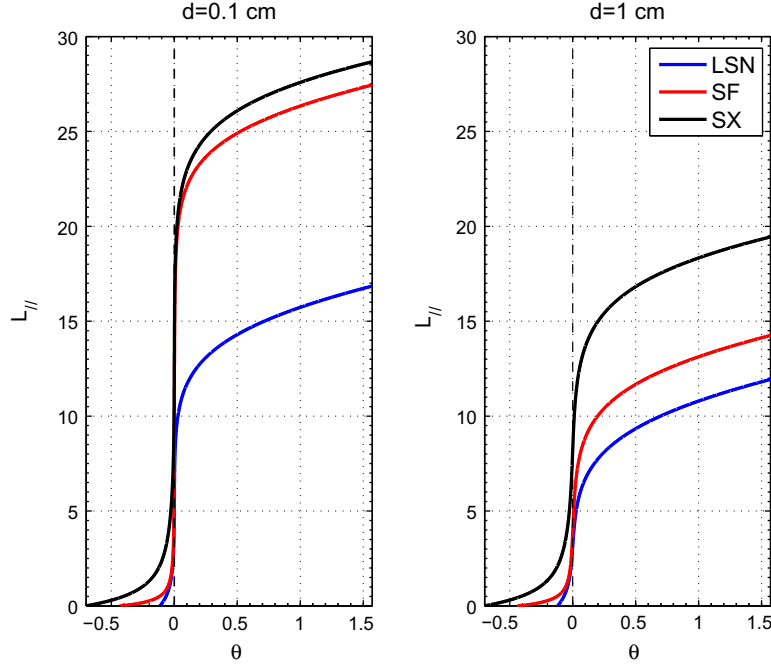


Fig. 2. Connection length for different configurations and different distances from the separatrix as a function of the poloidal angle.

3. Geometry and equilibrium

3.1. Operators

The Cauchy problem formed by the second order differential equation Eq. (5) and the boundary conditions Eq. (6) is well defined once the equilibrium quantities are fixed. In order to do that, we need to express k_{\perp}^2 , $\mathbf{k}_{\perp} \cdot \mathbf{b}_0 \times \boldsymbol{\kappa}$ and the operator $\mathbf{k}_{\perp} \cdot \mathbf{b}_0 \times \nabla_{\perp}$. We start by writing the equilibrium field: $\hat{\mathbf{b}}_0 = \mathbf{e}_{\zeta} + \mathbf{e}_{\chi} \times \nabla \Psi = q \nabla \Psi \times \nabla \theta + \nabla \zeta \times \nabla \Psi$, where $\hat{\mathbf{b}}_0 \equiv \mathbf{B}/B_{\zeta} = \mathbf{b}_0 B/B_{\zeta} \approx \mathbf{b}_0$ as $B/B_{\zeta} \approx 1$, θ and ζ are the poloidal and toroidal angles, \mathbf{e}_{ζ} is directed along ζ and has unity norm. The parameter $q = \frac{\hat{\mathbf{b}}_0 \cdot \nabla \zeta}{\mathbf{b}_0 \cdot \nabla \theta}$ is the local safety factor. With this convention, we have that $\partial \Psi / \partial x = b_y$ and $\partial \Psi / \partial y = -b_x$ and we can define $b_p \equiv |\mathbf{B}_p|/B_{\zeta} = \sqrt{b_x^2 + b_y^2} \ll 1$, where \mathbf{B}_p is the poloidal magnetic field.

We evaluate \mathbf{k}_{\perp} as in ballooning theory by imposing the following conditions [14]: (1) $\mathbf{k}_{\perp} = N \nabla S$; (2) $\mathbf{b}_0 \cdot \mathbf{k}_{\perp} = N \nabla_{||} S = 0$; (3) $\mathbf{e}_{\zeta} \cdot \mathbf{k}_{\perp} = N$. Here N is an integer number determining the amplitude of the wave vector and condition (1) corresponds to $\nabla \times \mathbf{k}_{\perp} = 0$. This leads to: $\mathbf{k}_{\perp}/N = \nabla \zeta - v \nabla \theta + (\beta_k - \beta_{k,0}) \nabla \Psi$, where $\nabla_{||} \beta_k = -\frac{1}{q} \frac{\partial q}{\partial \Psi} = -\hat{s}$, \hat{s} is the local magnetic shear and $\beta_{k,0}$ is an integration constant that determines the direction of the wave vector.

By writing $\nabla f_{eq} = \frac{\partial f_{eq}}{\partial \Psi} \nabla \Psi + \frac{\partial f_{eq}}{\partial \theta} \nabla \theta + \frac{\partial f_{eq}}{\partial \zeta} \nabla \zeta$, we find: $\mathbf{k}_{\perp} \cdot \mathbf{b}_0 \times \nabla f_{eq} = -N \frac{\partial f_{eq}}{\partial \Psi} - N(\beta_k - \beta_{k,0}) \frac{\partial f_{eq}}{\partial \zeta}$, where χ is the bi-normal coordinate, such that $\frac{\partial f_{eq}}{\partial \chi} \approx \frac{1}{q} \left(\frac{\partial f_{eq}}{\partial \theta} - q b_p^2 \frac{\partial f_{eq}}{\partial \zeta} \right)$.

Finally, in low β plasmas $\boldsymbol{\kappa} \approx \nabla_{\perp} B/B$ with $B \sim R^{-1}$. This gives $\boldsymbol{\kappa} \approx -\mathbf{e}_{\chi}$ and $\mathbf{b}_0 \times \boldsymbol{\kappa} \approx -\mathbf{e}_y + b_y \mathbf{e}_{\zeta}$, from which the curvature operator can be calculated [14].

3.2. Magnetic field and equilibrium parameters

The equilibrium magnetic field is generated using straight current carrying wires representing the plasma current and the

divertor coils. This has the advantage of giving simple analytic expressions for the magnetic flux, $\Psi = C \log(r_p r_{d1}^{\alpha_1} r_{d2}^{\alpha_2})$, and the poloidal angle, $\theta = \text{atan} \left(\frac{y-y_p}{x-x_p} \right) + \alpha_1 \text{atan} \left(\frac{y-y_{d1}}{x-x_{d1}} \right) + \alpha_2 \text{atan} \left(\frac{y-y_{d2}}{x-x_{d2}} \right) + c_1$.

Here $r_p \equiv \sqrt{(x-x_p)^2 + (y-y_p)^2}$ is the distance between a point and the wire representing the plasma, which is at $[x=x_p, y=y_p]$ (the distance to the divertor coils is defined similarly), $\alpha_{1,2}$ are the ratio between the divertor coils and the plasma currents and c_1 is a constant used to fix the angle of the X-point at $\theta = 0$. With this convention, the angle θ is $\pi/2$ at the outer midplane, π at the top of the tokamak, 0 and 2π at the X-point (at the low and high field side, respectively), $-\theta_{d0}$ at the outer target and $2\pi + \theta_{di}$

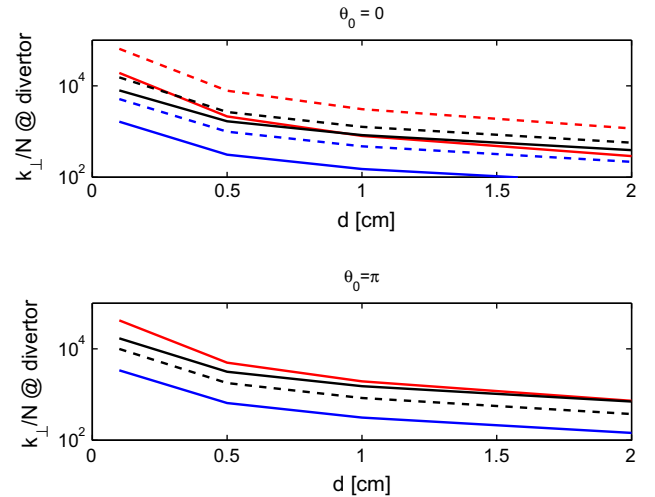


Fig. 3. Modulus of the perpendicular wave number as a function of the distance from the separatrix for different θ_0 and divertor configuration. The blue, red and black curves represent LSN, SF and SX respectively. The solid lines are for the outer divertor and the dashed for the inner divertor. (For interpretation of the references to color in this figure legend, the reader is referred to the web version of this article.)

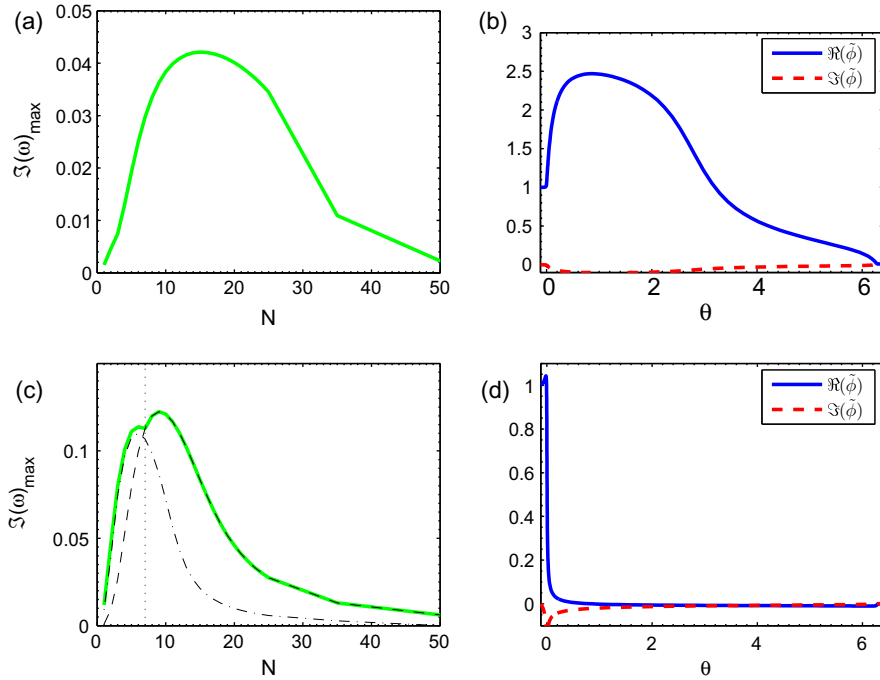


Fig. 4. Maximum growth rate and mode structure for LSN $d = 0.5$ cm, $\lambda = 1$ cm, plots (a) and (b), and for $d = 0.1$ cm, plots (c) and (d). In plot (c) the vertical dotted line shows the transition between weakly ballooned modes (b) and divertor localized modes (d). The dashed-dotted and the dashed line represent the maximum growth rate of the former and latter modes.

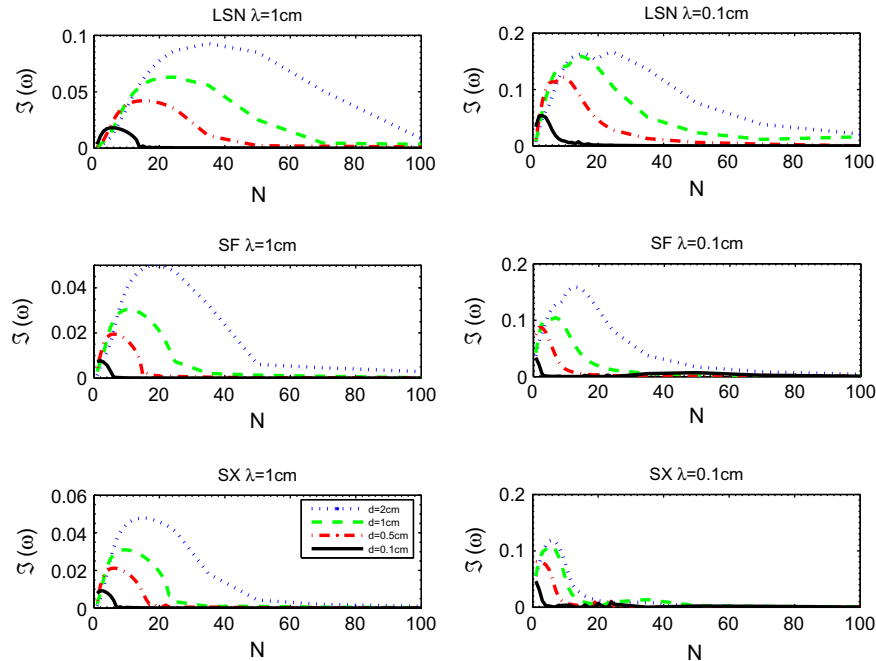


Fig. 5. Maximum growth rate as a function of N for all the configurations studied. Solid, dashed, dash-dotted and dotted lines represent d equal to 0.1 cm, 0.5 cm, 1 cm and 2 cm respectively.

at the inner target. The constant $C = \mu_0 I_p / (2\pi R B)$ determines the pitch angle of the field lines and for a circular tokamak would become $C \approx (a/R)^2 q_a^{-1}$ where a is the minor radius and q_a the safety factor there. We fixed $C = 3^{-3}$ representing an equivalent circular tokamak with an edge safety factor and aspect ratio of 3.

We studied three divertor configurations with Lower Single Null (LSN), exact Snowflake (SF) [11] and Super-X (SX) [12] geometry. The wires parameters for these configurations are

shown in Table 1 ($x_p = 0$ in all cases) and the geometry of the field is represented in Fig. 1. In the simulations, we assumed a deuterium plasma ($Z = 1$, $A = 2$) for ITER ($T_0 = 200$ eV, $n_0 = 2.5 \cdot 10^{13}$ cm $^{-3}$, $B = 5.3 \cdot 10^4$ G, $R = 600$ cm) relevant parameters [6] and assumed $\tau = 2$. In the three configurations, we compared the stability of field lines at four different distances from the separatrix, d , calculated at the outer midplane (where $B_x = 0$): 0.1 cm, 0.5 cm, 1 cm, 2 cm. The connection length (outer midplane

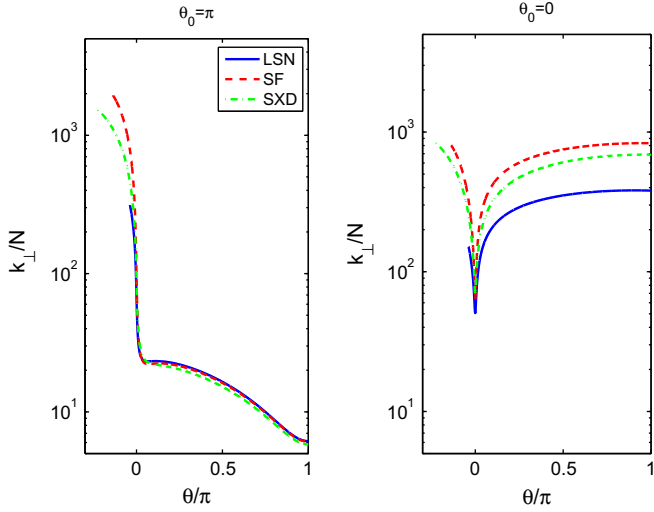


Fig. 6. Parallel profiles of $k_{\perp}/N = \mathcal{D}^{-1/2}$ at $d = 1$ cm for $\theta_0 = \pi$ (left) and $\theta_0 = 0$ (right).

to target distance), L_{\parallel} , is longer for the SF and SX configurations with respect to the LSN, as shown in Fig. 2. Note that in all the simulations the divertors are in the sheath limited regimes (i.e. small collisionality $v_* \lesssim 10$), thus justifying an equilibrium with no parallel variations. Hence, we take an equilibrium with an exponential decay in Ψ and no variation along χ and s , such that $dn_{eq}/d\Psi \approx \delta\beta b_p^{-1} \lambda_n^{-1}$ and $dT_{eq}/d\Psi \approx b_p^{-1} \lambda_T^{-1}$, where $\lambda_{n,T}$, which are the decay length of the fields n and T (measured in cm and normalized to R), and b_p are evaluated at the outer midplane (where $\partial f_{eq}/\partial y = 0$). In the calculations presented here we assumed $\lambda = \lambda_n = \lambda_T$ and investigated decay lengths equal to 0.1 cm and 1 cm.

The effect of the magnetic shear is taken into account by the parallel variation of \mathbf{k}_{\perp} . In Fig. 3, we plot k_{\perp}/N as a function of d for the three configurations and for θ_0 equal to 0 and π . Note that θ_0 is the value of the poloidal angle at which $\beta_k = \beta_{k,0}$ and hence

determines the direction of \mathbf{k}_{\perp} . The curves in Fig. 3 show that, with respect to the LSN configuration, the SF and SX divertors produce stronger shearing at the target because of the effect of the X-point region on the former and the longer divertor leg length on the latter. This has consequences on the stability of the mode as well as on the estimated diffusivity.

4. Numerical results

We solved numerically Eq. (5) with the boundary condition Eq. (6) and the equilibria discussed in the previous Section. In order to do that, we used a shooting code benchmarked with analytic solutions (obtained assuming constant k_{\perp}) and with the non resistive results in [10]. By systematically exploring the (N, θ_0) space, we identified the most unstable modes for each N , divertor configuration and plasma equilibrium.

We started by addressing the effect of a narrow SOL width. Our “large” SOL case, $\lambda = 1$ cm, produced results largely consistent with those presented in [10]: maximum growth rate around $\theta_0 = \pi$, with a broad maximum in θ_0 ; mode stabilization due to partial line tying at low N and due to diamagnetic effects at large N , see Fig. 4(a); a weakly ballooned mode structure, mildly localized on the outer region, see Fig. 4(b); mode driven by curvature and sheath effects [9]. Not surprisingly, the steeper gradient increases the growth rate of the modes, Fig. 4(c), but also leads to an unexpected change in their nature. For all d , a gradual reduction of the decay lengths shows initially a shift of the maximum value of the growth rate towards lower values of θ_0 and then the appearance of a mode localized in the outer divertor leg, Fig. 4(d), which becomes dominant when $\lambda \approx 0.1$ cm. In the $[N, \theta_0]$ space, this perturbation is localized in a narrow band around $\theta_0 \approx 0$ and it reaches its maximum growth rate for values on N larger than the still present weakly localized mode (see Fig. 4(c)).

The stability of the mode changes significantly depending on the radial position in the SOL. In all our simulations, the farther the field line is from the separatrix, the larger the maximum growth rate, which is also achieved at higher N values, see Fig. 5. This can be explained by the fact that close to the separatrix, k_{\perp}

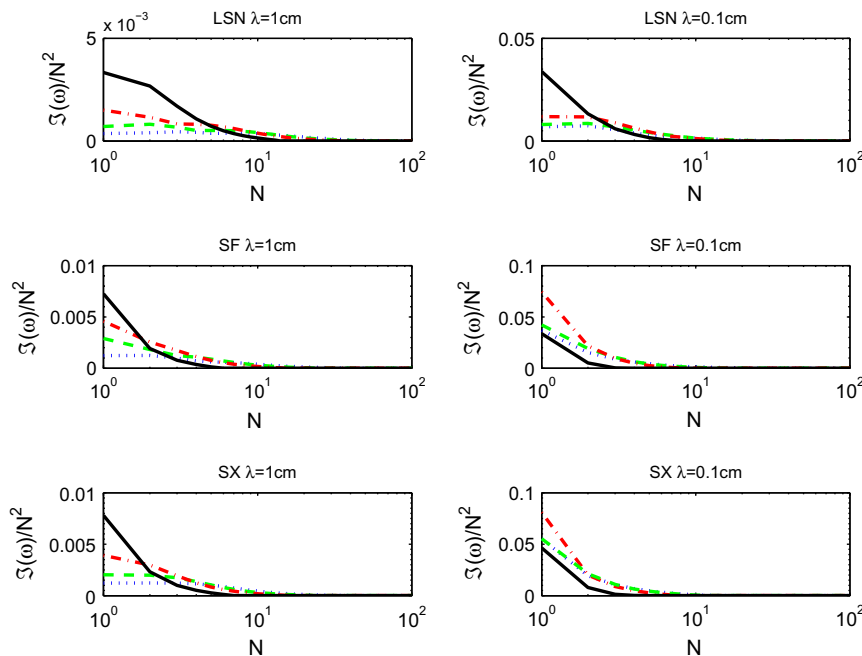


Fig. 7. $\Im(\omega)/N^2$ as a function of N for all the configurations studied. Line styles as in Fig. 5.

at the target becomes large (see Fig. 3), thus reducing the incomplete line tying stabilization, that goes like $1/k_{\perp}^2$ [10] and the sheath drive term [9]. For the same reason, Snowflake and Super-X divertors, which have higher perpendicular wave number at the target, show a similar trend for $\Im(\omega)$, see Fig. 5.

We define the estimated diffusion coefficient as $D \sim \Im(\omega)/k_{\perp}^2 = \mathcal{D}(s)\Im(\omega)/N^2$, where $\mathcal{D}(s)$ determines its parallel variation and depends exclusively on the magnetic geometry, see Fig. 6. The quantity $\Im(\omega)/N^2$ is plotted in Fig. 7 for the cases studied and shows recognizable trends. Comparing the left and the right columns of Fig. 7 shows that higher SOL gradients systematically increase the diffusion coefficient. This happens roughly in a linear way for $d \leq 1$ cm and low N , while the increase is weaker for higher N . For $\lambda = 0.1$ cm and sufficiently large N , the divertor modes discussed above contribute to the transport together with the weakly ballooned modes, so that we expect a local enhancement of the turbulence and the transport in the outer divertor leg.

In advanced divertors, $\Im(\omega)/N^2$ increases around a factor 2 with respect to LSN, Fig. 7. Only close to the separatrix and for steep gradients (i.e. $d = 0.1$ cm, $\lambda = 0.1$ cm) we find no increase in the estimated diffusion. Snowflake and Super-X configurations behave similarly despite the fact that the longer connection length and magnetic fanning are obtained in different ways (in the X-point region for the former, in the long outer divertor leg for the latter). However, to have a complete picture, also parallel variations (i.e. \mathcal{D}) must be taken into account, Fig. 6. While LSN, SF and SX configurations have similar \mathcal{D} above the X-point for the dominant weakly ballooned mode, close to the target they change significantly with LSN reaching much larger values of $\mathcal{D} = (N/k_{\perp})^2$ than SF or SX, as shown in Figs. 3 and 6. This suggests that transport in advanced configuration might increase in the midplane region, but be reduced in the proximity of the target. In other words, the longer connection length below the X-point does not significantly increase the plasma spreading in the divertor region because the in the extra length the diffusion coefficient reduces. However, the small perpendicular size of the perturbations beyond the X-point might induce secondary instabilities in the nonlinear phase, which might change the transport estimates.

5. Conclusions

We calculated the stability of an ITER like Scrape Off Layer to ideal curvature and sheath driven flute perturbations. We found that steep gradients can destabilize a divertor localized mode and increase the diffusion coefficient. For all magnetic geometries, this could have the beneficial effect of spreading the SOL width below the X-point, thus alleviating the divertor heat loads. We also compared standard Lower Single Null to Snowflake and Super-X configurations. We showed that the increased shearing of the mode in the advanced configurations reduces the maximum growth rate of the instabilities. With respect to standard configurations, the upstream diffusion coefficient doubles, although in the divertor region the much larger perpendicular wave number imply

that in advanced configurations the turbulent diffusion due to the weakly ballooned mode below the X-point is increased only marginally. Experimental evidence shows filaments ejected from the separatrix in both L-mode and in the inter-ELM phase [5]. The transport due to these structures, which could account for 50–60% of the total [5] (the rest is due to the intrinsic instabilities and neoclassical effects), is not discussed in this paper and might compensate the reduced diffusive coefficient due to the intrinsic instabilities in advanced configurations. However, the question of how the intermittent transport is affected by steeper gradients or advanced divertor configurations is still open [15].

Our work addresses the problem rigorously within the framework of the model used. However, a number of approximations were made and a few comments are appropriate. The extreme shearing of the mode in the divertor region would call for a kinetic treatment of the problem, at least in the close proximity of the separatrix. For the ITER simulations, however, ρk_{\perp} exceeds unity only in advanced configurations when considering regions very close to the divertor and very close to the separatrix (i.e. $\theta_0 \approx -\theta_{d0}$ and $d = 0.1$ cm). The linear approximation used here is likely to be able to give only a qualitative understanding of the problem as fluctuations are typically large in the SOL. Extensions of the model, such as the introduction of more complete equations for the density and temperature evolution, as well as the effect of parallel advection are envisaged and expected to play a role. The analysis of fully toroidal configurations in higher collisionality regimes (i.e. high recycling and detached conditions) is left for future work.

Acknowledgements

This work was funded by the RCUK Energy Programme [Grant No. EP/I501045] and by the European Union's Horizon 2020 research and innovation programme. To obtain further information on the data and models underlying this paper please contact PublicationsManager@ccfe.ac.uk. The views and opinions expressed herein do not necessarily reflect those of the European Commission.

References

- [1] ITER Physics Basis Editors, Nucl. Fusion 39 (1999) 2137.
- [2] A. Loarte, B. Lipschultz, A.S. Kukushkin, et al., Nucl. Fusion 47 (2007) S203.
- [3] T. Eich, B. Sieglin, A. Scarabosio, et al., PRL 107 (2011) 215001.
- [4] V. Naulin, J. Nucl. Mater. 363–365 (2007) 24.
- [5] D.A. Dippolito, J.R. Myra, S.J. Zweben, Phys. Plasmas 18 (2011) 060501.
- [6] F. Militello, W. Fundamenski, Plasma Phys. Control. Fusion 53 (2011) 095002.
- [7] D. Farina, R. Pozzoli, D.D. Ryutov, Nucl. Fusion 33 (1993) 1315.
- [8] X. Garbet, L. Laurent, J.P. Roubin, A. Samain, Nucl. Fusion 31 (1991) 967.
- [9] H.L. Berk et al., Nucl. Fusion 33 (1993) 263.
- [10] J.R. Myra, D.A. Dippolito, J.P. Goedbloed, Phys. Plasmas 4 (1997) 1330.
- [11] D.D. Ryutov, Phys. Plasmas 14 (2007) 064502.
- [12] P.M. Valanju, M. Kotschenreuther, S.M. Mahajan, J. Canik, Phys. Plasmas 16 (2009) 056110.
- [13] A.S. Kukushkin et al., J. Nucl. Mat. 438 (2013) S203–S207.
- [14] R.D. Hazeltine, J.D. Meiss (Eds.), Plasma Confinement, Dover Publications, New York, 1992. ISBN 0-486-43242-4.
- [15] F. Militello, W. Fundamenski, V. Naulin, A.H. Nielsen, Plasma Phys. Control. Fusion 54 (2012) 095011.